Journal of Materials Chemistry A

ROYAL SOCIETY OF CHEMISTRY

PAPER

View Article Online
View Journal | View Issue

Cite this: J. Mater. Chem. A, 2024, 12, 20077

Electrochemical reduction of nitrate to ammonia on ultra-stable amorphous Co–P electrocatalyst†

Jin-Long Fan, [a] Sheng-Bo Liu,[c] Ming-Liang Chen,[d] Zhangxiong Wu, [a] Sheng-Peng Sun*[a] and Yao-Yin Lou *[ab]

Electrocatalytic reduction of nitrate (NO_3^-) to ammonia (NH_3) is garnering increasing interest due to its potential to reduce CO_2 emissions as a substitute for the Haber-Bosch process, while also mitigating NO_3^- pollution. However, it remains a challenge to achieve a current density exceeding 300 mA cm^{-2} while maintaining the stability of catalysts. Additionally, the anodic oxygen evolution reaction, characterized by slow kinetics and high energy barriers, severely impedes the widespread adoption of NH_3 formation from NO_3^- reduction. Therefore, in this study, we introduce amorphous phosphorus-doped cobalt catalysts (Co–P@NF) prepared *via* a facile electrodeposition process for efficient NO_3^- reduction and hydrazine oxidation. The incorporation of phosphorus in Co–P@NF facilitates electron migration from phosphorus to cobalt, enhancing *H provision for efficient hydrogenation of the intermediate $*NO_2^-$. This results in a current density of 2 A cm^{-2} at −0.3 V, with a faradaic efficiency for NH_3 of 91% in an electrolyte containing 1 M NO_3^-. Moreover, the Co–P@NF catalyst exhibits remarkable long-term stability, maintaining an NH_3 faradaic efficiency exceeding 90% and a current density of 799 mA cm^{-2} after 82 hours of electrolysis. Furthermore, Co–P@NF displays high catalytic activity in promoting the rate-determining step of hydrazine oxidation, from $*N_2H_2$ to $*N_2H$. The incorporation of the HzOR (hydrazine oxidation reaction)-assisted NO_3^-RR (nitrate reduction reaction) unit significantly reduces the cell voltage to 0.34 V at 300 mA cm^{-2}.

Received 4th April 2024
Accepted 13th June 2024

DOI: 10.1039/d4ta02299h

rsc.li/materials-a

[a]School of Chemical and Environmental Engineering, College of Chemistry, Chemical Engineering and Materials Science, Soochow University, Suzhou, Jiangsu 215123, China. E-mail: shepsun@suda.edu.cn; yylou@iue.ac.cn

[b]CAS Key Laboratory of Urban Pollutant Conversion, Institute of Urban Environment, Chinese Academy of Sciences, Xiamen 361021, P. R. China

[c]Jiangsu Key Laboratory of Environmental Science and Engineering, School of Environmental Science and Engineering, Suzhou University of Science and Technology, Suzhou 215009, China

[d]Department of Chemical Engineering, Delft University of Technology, Van der Maasweg 9, Delft, 2629HZ, the Netherlands

† Electronic supplementary information (ESI) available. See DOI: https://doi.org/10.1039/d4ta02299h

Yao-Yin Lou

Yao-Yin Lou earned his PhD degree in 2019 from Ecole Nationale Supérieure de Chimie de Rennes, France, where he received joint training from Université de Rennes 1. From 2020 to 2022, he served as an associate researcher at Xiamen University and subsequently worked as an associate professor at Soochow University. Presently, he is a professor at the Institute of Urban Environment, Chinese Academy of Sciences. His research focuses on the development of novel environmental electrocatalysts and electroreduction methods for the elimination of environmental contaminations. Dr Lou has authored over 30 papers in renowned international journals such as Nature Communications, ACS Catalysis, Environmental Science & Technology, Water Research, and Chemical Engineering Journal.

1. Introduction

Ammonia (NH_3) is a vital chemical utilized in various industrial applications, such as chemical production, fuel synthesis, and as a fertilizer. Approximately 50% of global food production depends on NH_3 fertilizers.[1] The industrial-scale production of NH_3 predominantly relies on the Haber-Bosch process, which operates at high temperatures (400–600 °C) and high pressures (200–350 atm).[2] This production process is responsible for approximately 1.2% of annual global CO_2 emissions, surpassing emissions from other industrial chemical processes.[3] To address decarbonization challenges in the ammonia sector, an alternative approach known as the dinitrogen reduction reaction has been developed [4]. However, the dinitrogen reduction reaction exhibits a significantly low reaction rate (<10 mmol g_{cat}^{-1} h^{-1}),[2] which is two to three orders of magnitude lower than that of the Haber-Bosch process. In marked contrast, nitrate anions (NO_3^-) require only 204 kJ mol^{-1} of energy to break the N=O bond, a significantly lower energy requirement compared to the N≡N bond in dinitrogen gas (941 kJ mol^{-1}). Additionally, NO_3^- anions exhibit excellent solubility in aqueous solutions.[4] Consequently, the electrochemical reduction reaction of NO_3^- (NO_3^-RR) for NH_3 production has garnered increasing attention.

NO_3^- pollution is a pressing environmental issue, resulting from agricultural runoff, wastewater discharge, and industrial processes. It poses risks to human health and ecosystems, making the development of effective NO_3^- removal strategies critical. The electroreduction of NO_3^- aims to produce ammonia, serving the dual purpose of recycling waste materials and mitigating the adverse environmental and ecological impacts of excessive NO_3^- discharge.[5] Thanks to these advantages, various metal-based electrocatalysts, including Cu, Ru, Ag, Fe, Pd, and Co, have been developed to facilitate the reduction of NO_3^- to NH_3.[2,6,7] However, the reduction of NO_3^- to NH_3 is a complex eight-electron reaction (eqn (1)), inevitably resulting in the formation of undesired byproducts such as nitrogen oxyanions and dinitrogen.[8,9] Due to significant progress in electrocatalyst development, achieving high faradaic efficiencies towards NH_3 (FE_{NH_3} > 90%) is feasible at pseudo-ampere-lever current densities. Nevertheless, the long-term stability of catalysts operating at currents exceeding 300 mA cm^{-2} with FE_{NH_3} > 90% remains challenging, falling short of the standards set by the U.S. Department of Energy.[10] Meanwhile, the anodic oxygen evolution reaction (OER, $2OH^- \rightarrow H_2O + 1/2O_2 + 2e^-$, 1.23 V *vs.* RHE), suffers from slow reaction kinetics and high energy barriers, necessitating an applied potential exceeding 1.6 V.[11] The high voltage requires substantial energy expenditure thereby significantly restricting the widespread application of NH_3 formation from NO_3^- reduction. Substituting sluggish reactions with thermodynamically favorable ones, such as hydrazine oxidation reaction (HzOR, $N_2H_4 + 4OH^- \rightarrow N_2 + 4H_2O + 4e^-$, −0.33 V *vs.* RHE), to assist NO_3^-RR could greatly lower the electricity consumption for NH_3 formation. Moreover, the employment of HzOR-assisted NO_3^-RR offers environmental benefits, converting toxic, carcinogenic N_2H_4 in wastewater into dinitrogen and water. Developing bifunctional electrocatalysts toward anodic HzOR and cathodic NO_3^-RR with high activity and durability is pivotal to promote the practical applications.

$$NO_3^- + 6H_2O + 8e^- \rightarrow NH_3 + 9OH^-, \quad pH = 14,\ E^\circ = 0.69\ V\ vs.\ RHE \tag{1}$$

NO_3^-RR is a typical hydrodeoxygenation reaction. Electrocatalysts, like the first-row transition metal phosphides, with good performance in hydrogen evolution and hydrogenation reactions have been reported to have good NO_3^-RR catalytic activities.[2,6] Javier Vela *et al.*[12] found that over 96% selectivity of NH_3 from NO_3^- reduction was achieved on Ni_2P, which was previously reported as a good electrocatalyst for hydrogen evolution reaction (HER).[13] Yang *et al.*,[14] found that the Co nanocrystals that could generate plenty of *H had an exceptional performance of electrochemical NO_3^-RR to NH_3. Li *et al.*[15] also proved that the generated *H with moderate adsorption energy on the catalyst can behave as important reactive species for the hydrogenation of reaction intermediates to NH_3 and suppress the competing HER. Notedly, the good modulation of the adsorption energy of *H and *NO_3 on the catalyst surface is critical for the improvement of the catalytic activity and product selectivity.[16] Meanwhile, a synergistic benefit was also proposed by Simpson and Johnson for the CuNi alloys: the Ni sites acted as the active sites for the adsorption of *H, and the Cu sites facilitated the adsorption of NO_3^- intermediates on these binary alloy electrodes.[17]

On the other hand, amorphous materials with long-range disordered structures have exhibited superior electrocatalytic performance and durability compared to their crystalline counterparts.[18,19] The coordination of surface atoms on amorphous materials is highly unsaturated. Also, amorphous alloy has a high degree of structure flexibility, both of which benefit catalysis. Due to the advanced properties, the amorphous-structure catalysts were widely used in oxygen reduction,[20] carbon dioxide reduction,[21] and hydrogen evolution reaction.[22] However, to our best knowledge, few literature reports exist on the amorphous catalysts for the NO_3^-RR process. Inspired by the exceptional performance of the Co-based catalyst for HER and hydrodeoxygenation reaction,[23] the amorphous Co–P was prepared *via* a facile one-step electrodeposition procedure for HzOR-assisted NO_3^-RR. The as-prepared amorphous Co–P exhibited superior catalytic performances, which is one of the most advanced NO_3^-RR catalysts so far, as (1) a high partial current density for NH_3 formation (j_{NH_3}) was observed at 2 A cm^{-2}, along with a faradaic efficiency (FE_{NH_3}) of 91% at −0.3 V *versus* RHE. The corresponding yield of NH_3 production was 2.9 mol g_{cat}^{-1} h^{-1}, which is almost 11-fold higher than that achieved by the Haber-Bosch process (200 mmol g_{cat}^{-1} h^{-1}); (2) a good stability for NH_3 formation with FE_{NH_3} over 90% at current density around 800 mA cm^{-2} for more than 82 h electrolysis; (3) the cell voltage of HzOR-assisted NO_3^-RR at 300 mA cm^{-2} over Co–P@NF‖Co–P@NF was only 0.34 V. Electrochemical *in situ* shell-isolated nanoparticle enhanced Raman spectroscopy (SHINERS) was conducted to clarify the pathways and mechanisms of NO_3^-RR.

2. Materials and methods

2.1. Materials

Nickel foam (NF) used as electrode substrate was supplied from Suzhou JiaShide Foam Metal Co., Ltd. Trisodium citrate dihydrate ($C_6H_5Na_3O_7 \cdot 2H_2O$) and sodium hypophosphite ($NaH_2PO_2 \cdot H_2O$) were obtained from Meryer Chemical Technology Co., Ltd. $CoCl_2 \cdot 6H_2O$, KOH and $(NH_4)_2SO_4$ were purchased from Sinopharm Chemical Reagent Co., Ltd. $NaNO_3$ and $NaNO_2$ were bought from Aladdin Co., Ltd. All reagents were analytical grade without any further purification and all solution were prepared by Milii-Q water (MQ).

2.2. Synthesis of Co@Ni foam and Co–P@Ni foam

Phosphorus doped cobalt on the Ni foam substrate (Co–P@NF) was prepared by a simple constant-potential electrodeposition method in a three-electrode system, where Ni foam, Pt foil, and saturated calomel electrode (SCE) were applied as the working electrode, counter electrode and reference electrode, respectively. Before the electrodeposition process, Ni foam (0.5×1.0 cm^2) was ultrasonically cleaned in acetone solution, ethanol solution and deionized (DI) water several times. An aqueous solution (55 mL) containing 0.2 M $C_6H_5Na_3O_7$, 0.5 M $(NH_4)_2SO_4$, 0.6 M NaH_2PO_2 and 0.1 M $CoCl_2 \cdot 6H_2O$ were used as the electrolyte. Co–P was deposited on the Ni foam at −2.0 V *vs.* SCE in the above electrolyte saturated with N_2 at room temperature for 45 min. The preparation of Co@NF followed the same process but without the addition of NaH_2PO_2.

2.3. Assembly of Zn–nitrate flow battery

The Zn–nitrate flow battery was assembled in a membrane electrode assembly flow reactor wherein Co–P@NF (2 cm × 2 cm) was used as both the anode and cathode, respectively. The anodic and cathodic chambers were separated by a Nafion N115 proton exchange membrane. Bipolar plates were high-purity titanium plates with a single serpentine flow field and guard plates were Perspex sheets. The catholyte was 1 M NaOH/0.1 M KNO_3 while the anolyte was 6 M NaOH, and their flow rates were controlled to be 150 mL min^{-1} by a peristaltic pump. Chronopotentiometry was recorded to plot the polarization curves. The power density (P) was calculated by the following equation: $P = j \times E$, where j is the current density and E is the cell voltage.

2.4. Electrochemical measurements

The electrocatalytic performances of Co@NF and Co–P@NF were investigated in a three-electrode system connected to a DH7000C electrochemical workstation (Donghua, Jiangsu) in an H-type cell with a Nafion 115 membrane as a separator. The Co@NF and Co–P@NF with the same size (0.5×0.5 cm^2) were used as working electrodes, while a platinum foil and a saturated calomel electrode were used as the counter electrode and reference electrode. 1 M KOH aqueous solution (30 mL) containing different $NaNO_3$ concentrations (*i.e.*, 10, 20, 50, 100 and 1000 mM) and 1.0 M N_2H_4 were used as the cathodic and anodic electrolyte, respectively. The electrochemical linear voltammetry (LSV) analysis was carried out in a single undivided electrochemical cell. The Tafel slope was obtained by fitting the liner part of the Tafel plots according to the Tafel equation ($\eta = a + b \times \log(j)$). The electrochemical impedance measurement was performed in a frequency range of 0.01 Hz to 1000 Hz with an amplitude of 5 mV. The double layer capacitance (C_{dl}) of the obtained samples was calculated from CV curves at different scan rates of 10–100 mV s^{-1} in the non-Faraday area. The current density was normalized to the geometric electrode area (0.25 cm^2) unless otherwise specified. All recorded electrode potentials *vs.* Hg/HgO were transformed to potentials against the reversible hydrogen electrode (RHE) according to the calibration equation expressed as $E_{RHE} = E_{Hg/HgO} + 0.098 + 0.0591 \times pH$.

3. Results and discussions

3.1. Catalyst composition and microstructure

The Co–P@NF exhibits a much rougher surface than Co@NF (Fig. 1a and b), as indicated by the irregular nanograins formed on the surface of Co–P@NF (Fig. 1c), compared to the flat surface of Co@NF (Fig. 1d). As shown in the high-resolution transmission electron microscopy (HRTEM) images, the nanograins on Co–P@NF were amorphous (Fig. 1e), while the lattice fringe of Co@NF was observed (Fig. 1f). There was also no diffraction pattern for Co–P@NF, demonstrating the amorphous feature of this catalyst (Fig. S1†). The lattice distance of 1.91 Å was well ascribed to the (101) plane of metallic Co. The element mapping analysis (Fig. 1g) indicated that Co and P were evenly dispersed in the nanograins of Co–P@NF. The different structure morphologies of Co–P@NF and Co@NF were also confirmed by the XRD pattern (Fig. 1h). There was no crystalline peak observed in the XRD pattern of Co–P@NF, except the two peaks belonging to the Ni substrate. In comparison, two small peaks at 41.6° and 44.5° were observed in the XRD pattern of Co@NF, which were assigned to Co(100) and Co(101). The elemental compositions and electronic structure of Co–P@NF were determined using XPS (Fig. 1i and j). For Co–P@NF, P 2p showed a doublet with a binding energy of 128.3 (P $2p_{3/2}$) and 130.2 eV (P $2p_{1/2}$), assigned to elemental P (P^0) and oxidized P (P^{5+}), while Co 2p depicted two peaks at 781.8 eV (Co $2p_{3/2}$) and 797.6 eV (Co $2p_{1/2}$) assigned to oxidation of Co resulting from the exposition of the catalyst to air. There was no P 2p peaks found in the Co@NF spectra. It was well-fitted with the results from the HRTEM-EDS analysis. There were about 13 at% P in Co–P nanograins (Fig. S2 and Table S1†). Compared to Co–P@NF, the Co $2p_{3/2}$ and $2p_{1/2}$ peaks of Co@NF exhibited a small shift towards higher binding energies (Fig. 1i). This shift indicated that the introduction of P promotes electron migration from the P to the Co, which makes Co electron-rich and becomes more favorable for the NO_3^-RR processes. The electron-rich property of Co–P@NF was also demonstrated by EIS analysis (Fig. S3†). Thanks to the electron transfer from P to Co, the impedance of Co–P@NF (0.32 Ω) was lower than that of the Co@NF (0.52 Ω).

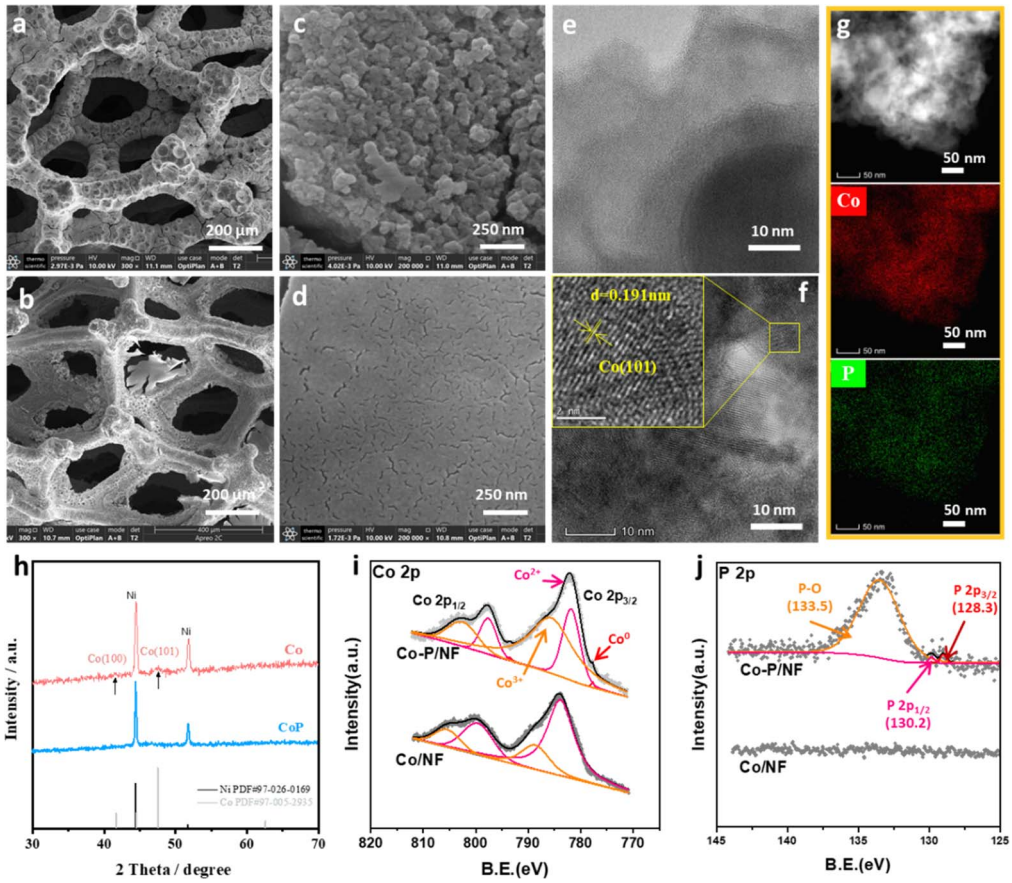

Fig. 1 SEM imagines of Co–P@NF (a and c) and Co@NF (b and d). HR-TEM imagines of Co–P@NF (e) and Co@NF (f). TEM-EDS mapping of Co–P@NF (g). (h) XRD pattern of Co–P@NF and Co@NF. XPS spectra: Co 2p (i) and P 2p (j) of Co–P@NF and Co@NF.

3.2. Electrocatalytic performances of NO_3^-RR

The linear sweeping voltammetry was firstly applied to investigate the catalytic activity over Co–P@NF and Co@NF during NO_3^-RR (Fig. 2a). In the absence of NO_3^-, Co–P@NF has a smaller onset potential (η_{HER}) and a much higher current density (j_{HER}) of hydrogen evolution reaction than that of Co@NF (η_{HER}: −0.05 V *vs.* −0.15 V; j_{HER} at −0.1 V: 69 mA cm^{-2} *vs.* 12 mA cm^{-2}), indicating the superior catalytic activity of HER on Co–P@NF. The Tafel slop of HER over Co–P@NF (136 mV dec^{-1}) was also smaller than that of Co@NF (164 mV dec^{-1}) (Fig. 2b), demonstrating that Co–P@NF had a faster kinetic for HER and provided more *H for NO_3^- reduction, according to Volmer step ($H_2O + e^- \rightarrow {}^*H + OH^-$). In the presence of NO_3^-, increased current densities (j) were observed on both Co-based electrodes, since Co was a good candidate for NO_3^-RR. The larger j on Co–P@NF indicated the enhanced catalytic activity of NO_3^- reduction after the incorporation of P into Co. Two current reduction peaks were appearing after the addition of NO_3^-, 0.09 V and −0.03 V on the curve of Co–P@NF, and 0.01 V and −0.15 V on the curve of Co. According to previous studies,[24,25] the first peak was assigned to NO_3^- reduction into $^*NO_2^-$ following a 2-electrons transfer process (eqn (2)), while the second peak was allocated to the $^*NO_2^-$ reduction into NH_3 following a 6-electrons transfer process (eqn (3)).

$$NO_3^- + H_2O + 2e^- \rightarrow {}^*NO_2^- + 2OH^- \quad (2)$$

$$^*NO_2^- + 5H_2O + 6e^- \rightarrow NH_3 + 7OH^- \quad (3)$$

Co–P@NF displayed positive shifts of 80 mV for the $NO_3^- \rightarrow NO_2^-$ peak and 120 mV for the $NO_2^- \rightarrow NH_3$ peak, compared to Co@NF, suggesting a drop of the energy barrier of $^*NO_3^-$ reduction to NH_3 on Co–P@NF. According to the Tafel slop in the NO_3^--containing electrolyte, Co–P@NF (32 mV dec^{-1}) had a higher kinetic activity for NO_3^-RR than that of Co (160 mV dec^{-1}). EIS results also revealed the incorporation of P into Co would decrease the electron transfer resistance that was beneficial to facilitate NO_3^-RR process. The constant-potential electrolysis was performed and the partial current density of NH_3 formation (j_{NH_3}) at different applied potential was obtained (Fig. 2c). The concentration of NH_3 and NO_2^- formed was detected by colorimetric methods using a UV-vis absorbance spectrophotometer (DR3900) and ion chromatography (ICS-600), respectively (Text S1, Text S2, Fig. S4 and S5†). The substrate of NF was relatively inactive for NO_3^-RR (Fig. S6†), since the j_{NH_3} on Ni foam was only 7 mA cm^{-2}, compared with the electrodeposited Co-based catalysts (1296 mA cm^{-2} on Co–P@NF and 212 mA cm^{-2} on Co@NF). Significantly higher j_{NH_3} was obtained with Co–P@NF, surpassing 1 A cm^{-2} at potential

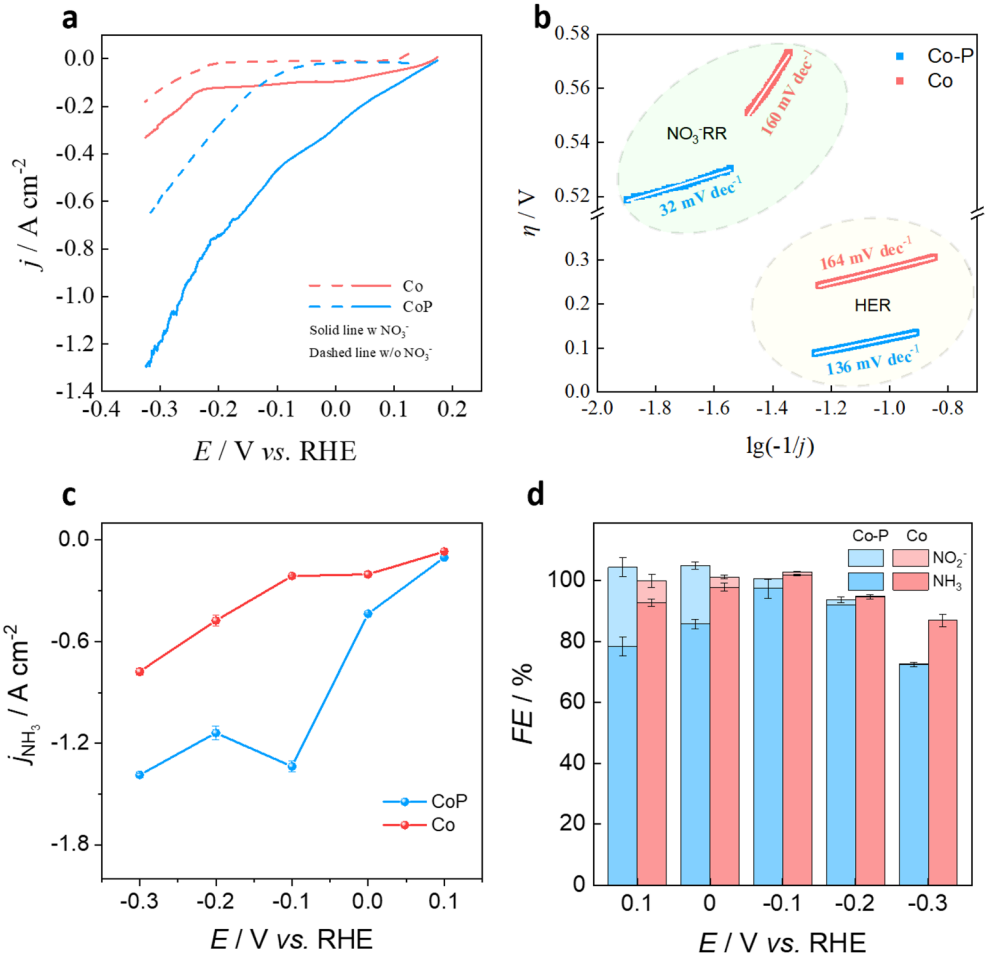

Fig. 2 (a) Linear sweeping voltammetry over Co@NF and Co–P@NF in the electrolyte of 1 mol L^{-1} KOH with or without 100 mmol L^{-1} NO_3^-. (b) Tafel slop of Co@NF and Co–P@NF in the presence of NO_3^-. (c) Partial current density of NH_3 production over Co@NF and Co-P@NF. (d) FE of NH_3 and NO_2^- over Co–P@NF and Co@NF in the potential range of 0.1–−0.3 V.

below −0.1 V *vs.* RHE. At this potential, the highest faradaic efficiency for NH_3 formation (FE_{NH_3}, 97.5%) was achieved with Co–P@NF (Fig. 2d). Consequently, the Co–P@NF electrode shows superior performance with high FE_{NH_3} and j_{NH_3} for NO_3^- electroreduction to NH_3 as compared to other reported electrodes, as exhibited in Table S2.† The low FE_{NH_3} over Co–P@NF at the potential of 0.1 V and 0 V, where the HER did not occur and the *H coverage (θ_H) was too low to further hydrogenation of NO_2^- to NH_3. Until the potential negatively shifted to −0.1 V, the θ_H increased, based on eqn (4), and therefore the maximum FE_{NH_3} was obtained. As potential continued to decreasing, the $FE_{NO_2^-}$ significantly declined but the slight decreased FE_{NH_3} was also observed due to the strong HER competition on the Co–P@NF (Fig. 2d). The competitive HER also led to a decrease in j_{NH_3} from 1336 mA cm^{-2} to 1138 mA cm^{-2}, when potential was negatively shifted from −0.1 V to −0.2 V. The electrochemically active surface area (ECSA) was also measured (Fig. S7a–c†), revealing that Co@NF and Co–P@NF had comparable ECSA. However, a higher ECSA-normalized current density for NH_3 production ($j_{NH_3(ECSA)}$) was observed with Co–P@NF (Fig. S7d†), indicating that this catalyst had higher intrinsic activity for NH_3 production. To clarify the possible N pollution caused by nitrogen reduction reaction, the electrolysis in the electrolyte free of NO_3^- ions was performed and little NH_3 was produced (Fig. S8†). j_{NH_3} in the solution with NO_3^- ions was over 133-fold higher than that in the electrolyte free of NO_3^-, where the FE_{NH_3} was only about 1%. In addition, the typical two peaks of $^{15}NH_4^+$ after the electrolysis of $^{15}NO_3^-$ also suggested that the NH_3 product indeed came from the electrocatalytic reduction of NO_3^- (Fig. S9†).

$$\eta = E - E_{eq} = \frac{RT}{F}\ln\frac{\theta_H}{\theta_H^0} \quad (4)$$

where θ_H and θ_H^0 are the *H coverage at E and E^o, respectively; F is the Faraday constant, 96 485C mol^{-1}; R is the gas constant, 8.314 J mol^{-1} K^{-1}; T is the kelvin temperature, K.

It should be noted that the sum FE of NO_2^- and NH_3 formation was over 100% (Fig. 2d). The NO_3^-RR over Co–P@NF and Co@NF were then performed at open circle potential (OCP) and the NO_2^- and NH_3 were both detected in the electrolyte (Fig. 3a and S10†), indicating that there was a spontaneous reduction of NO_3^- to NO_2^- and NH_3 on Co–P@NF and Co@NF.

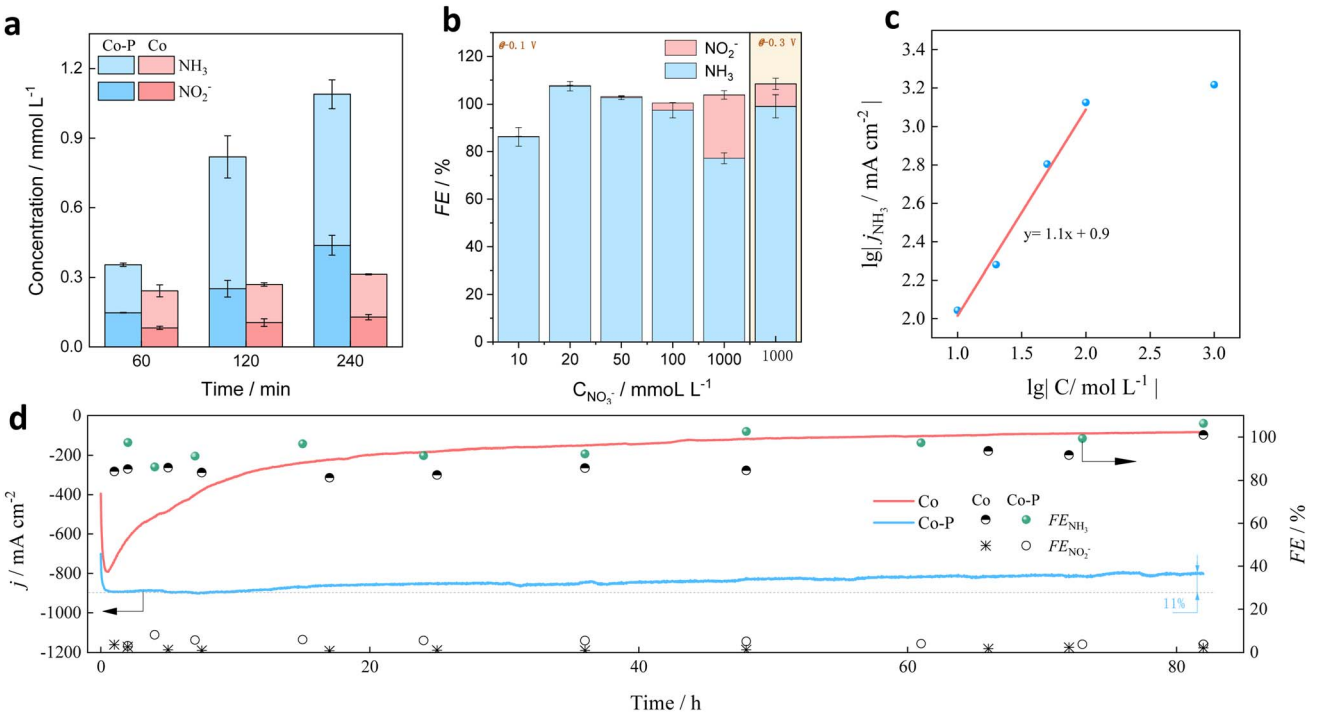

Fig. 3 (a) Concentration of NO_2^- and NH_3 over Co–P@NF and Co@NF at open circle potential. (b) FE of NO_2^- and NH_3 and (c) lg(–*j*) *vs.* lg *C* plots for Co–P@NF were calculated at −0.1 V *vs.* RHE. (d) Long-term stability of Co–P@NF in the electrolyte of 1 mol L^{-1} with 100 mmol L^{-1} NO_3^- at −0.1 V.

This spontaneous reduction process may explain the over-100% FE. A similar phenomenon was reported by Han and his colleagues:[26] oxidation of Co to $Co(OH)_2$ by NO_3^- (eqn (5)) and the electroreduction of $Co(OH)_2$ to Co (eqn (6)) proceed simultaneously during the NO_3^-RR (eqn (2) and (3)), and a dynamic Co valence cycle was achieved. The OCP over Co–P@NF was obviously lower than that of Co@NF (Fig. S11†), indicating that Co–P@NF had a superior ability of the spontaneous reduction of NO_3^-, thanks to the electron-rich of Co atom in Co–P@NF, giving that the NO_2^- and NH_3 formation on Co–P@NF was approximate 3-times higher than that of Co@NF at OCP.

$$NO_3^- + Co + H_2O \rightarrow {}^*NO_2^- + Co(OH)_2 \quad (5)$$

$$Co(OH)_2 + 2e^- \rightarrow Co + 2OH^- \quad (6)$$

The concentration of NO_3^- in real wastewater can vary from 1 mmol L^{-1} to 2000 mmol L^{-1}.[27] Therefore, NO_3^-RR on Co–P@NF was performed in a wide NO_3^- concentration range. The FE_{NH_3} was maintained above 95% in the range of 20 mmol L^{-1} to 100 mmol L^{-1} at −0.1 V (Fig. 3b). The low FE_{NH_3} in the solution of 10 mmol L^{-1} and 1000 mmol L^{-1} was due to the competitive adsorption between *H and $*NO_3$. For example, in the case of 10 mmol L^{-1}, NO_3^- concentration was so low that catalytic sites were occupied by *H which would be formed into H_2 *via* Volmer-Tafel or Volmer-Heyrovsky mechanism and decrease the FE_{NH_3}. When the NO_3^- concentration increased, the HER would be gradually hindered so that the $FE_{NO_2^-}$ increased. $FE_{NO_2^-}$ was about 27% in the case of 1000 mmol L^{-1} NO_3^-, where *H was insufficient for $*NO_2^-$ reduction (eqn (3)), leading to the accumulation of $*NO_2^-$ on the catalytic surface. A quasi-first-order reaction relationship between *j* and the NO_3^- concentration was obtained (Fig. 3c), revealing that the rate-determining step of NO_3^-RR ($RDS_{NO_3^-RR}$) was $NO_3^- \rightarrow NO_2^-$ step. Therefore, supplement of sufficient *H was significant for efficient reduction of NO_2^-. When a potential of −0.3 V was applied in the solution of 1000 mmol L^{-1}, an increase in FE_{NH_3} and a decrease in $FE_{NO_2^-}$ were observed, respectively. This is attributed to a higher θ_H (according to eqn (4)) and a stronger affinity of *H at more negative potentials,[28] which promotes further hydrogenation of NO_2^- to NH_3. Meanwhile, j_{NH_3} increased to 2 A cm^{-2} with the FE_{NH_3} as 91% (Fig. S12†). The corresponding NH_3 yield rate was 2.9 mol g_{cat}^{-1} h^{-1} that was almost 11-fold higher than that of Haber-Bosch route (200 mmol g_{cat}^{-1} h^{-1}). Long-term stability tests at −0.1 V *vs.* RHE assessed the durability of Co–P@NF against Co@NF (Fig. 3d). For Co–P@NF, FE_{NH_3} (>90%) remained stable after the 82 h electrolysis. The j_{NH_3} experienced a slight decrease from 890 mA cm^{-2} to 799 mA cm^{-2} (about 89% of the initial j_{NH_3}), which still exceeded U.S. Department of Energy's standard requirement by more than two fold (300 mA cm^{-2}). For Co@NF, the j_{NH_3} quickly decayed from 798 mA cm^{-2} to 198 mA cm^{-2} after 20 h electrolysis and its FE_{NH_3} was also lower than that of Co–P@NF. To further check the stability of the Co–P@NF catalyst, the cyclic electrolysis was also conducted for NO_3^- reduction. The results demonstrated that the faradaic efficiency of NH_3 formation remained consistently at 100% throughout the 11 electrolysis cycles. Moreover, the yield of NH_3 formation

of the 11th was still two-times higher than that of Haber-Bosch route (200 mmol g_{cat}^{-1} h^{-1}) (Fig. S13†). Above stability test results indicated the amorphous-structured Co@P indeed had a satisfactory durability during NO_3^-RR. According to the TEM analysis, the morphology of Co–P was well kept after the consecutive recycling tests (Fig. S14†). Furthermore, XRD (Fig. S15†) and XPS (Fig. S16†) analysis was also performed on the samples after the consecutive recycling tests, and the results demonstrated negligible changes in the chemical compositions and oxidation states. The excellent stability of the catalysts was possibly ascribed to amorphous feature of the Co–P catalysts.

Tert-butanol (TBA), used as a specific *H radical quenching reagent, was added during the process to evaluate the role of active *H (Fig. 4a). Upon the addition of TBA, the *j* decreased sharply from 546 mA cm^{-2} to 373 mA cm^{-2} on Co@NF and from 886 mA cm^{-2} to 628 mA cm^{-2} on Co–P@NF. Meanwhile, the FE_{NH_3} also decreased from 96% to 88% on Co@NF and from 106% to 100% on Co–P@NF. The quenching test results demonstrated that the *H radicals truly improved the reaction rate and FE_{NH_3}. We further used dimethyl-1-pyrroline-*N*-oxide (DMPO) as the radical trapping reagent to monitor the formation of *H radicals with and without using NO_3^- (Text S3). As shown in Fig. 4b, the ESR spectra display typical 9 signals with intensity ratios of 1 : 1 : 2 : 1 : 2 : 1 : 2 : 1 : 1 without adding NO_3^- in the catholyte, which confirms the formation of DMPO-H. When NO_3^- was added, the typical 9 signals nearly disappeared, indicating that the produced *H is consumed by the intermediates in the NO_3^-RR process. These results strongly prove the key role of the *H radicals in NO_3^- reduction into NH_3. The electrochemical *in situ* Raman spectra of Co–P and Co catalysts depicted in Fig. 4c and d, were recorded across a potential window of −0.7–−1.13 V *versus* the RHE with increments of 50 mV. Three distinct peaks, corresponding to A_{1g}, E_g and F_{2g} vibrations models of Co–O band, were visible on Co–P and Co catalysts at around 686.9, 480.5 and 524.9 cm^{-1}.[29] The formation of Co–O band was ascribed to the oxygen vacancies over the two catalysts. The coordination of surface atoms on amorphous materials is highly unsaturated.[30] According to the electron paramagnetic resonance (EPR) analysis (Fig. S17†), the Co–P@NF had a much higher density of

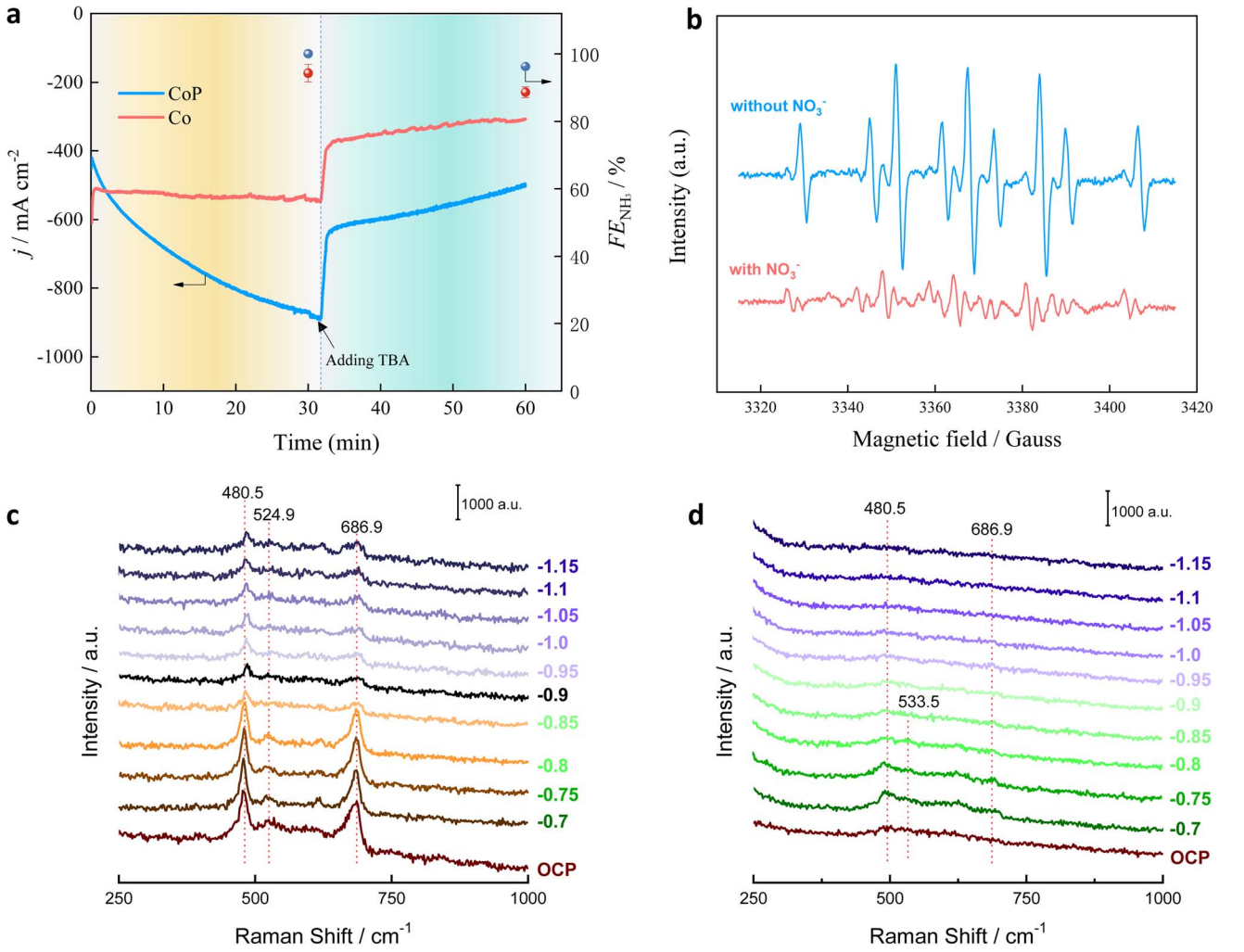

Fig. 4 (a) *j* and FE_{NH_3} over Co–P@NF and Co@NF at potential of −0.1 V *vs.* RHE. (b) The DMPO-H* obtained on Co–P@NF after 5 min of electrocatalysis at −0.1 V *vs.* RHE in 1 M KOH solution with 0.1 M NO_3^- (bottom) or (b) without NO_3^- (top). *In situ* electrochemical–Raman on Co–P (c) and Co (d) in the potential of −0.7 V–−1.15 V *vs.* Hg/HgO.

oxygen vacancies. The intensity of Co–O bands on Co–P was much higher than that Co. The Raman spectra were well fitting with the EPR results that the Co–P with amorphous structure had a higher density of oxygen vacancies. As the potential negatively shifted, the Co–O bands gradually decreased. For Co–P catalyst, the Co–O band could be preserved, revealing that the amorphous structure had more stable oxygen vacancies; while no signal could be observed on Co catalyst after the potential lower than −0.9 V. The oxygen vacancies can be used as the adsorption site for the charge transfer, which is conducive to the adsorption/desorption of the reaction intermediates speeding up the NO_3^-RR.[31]

3.3. Electrocatalytic performances of HzOR

The HzOR electrochemical performance of Co–P@NF was then evaluated in 1.0 M KOH + 1 M N_2H_4 electrolyte, compared to Co@NF and NF. Co–P@NF showed a higher HzOR catalytic activity with small overpotentials of −67, −16 and 486 mV to reach 10, 100 and 1000 mA cm^{-2} (Fig. 5a), respectively, compared to Co@NF and NF. The smallest Tafel slope of 24.2 mV dec^{-1} was obtained in Co–P@NF, indicating the favorable catalytic oxidation kinetics toward HzOR (Fig. 5b). This ultra-low Tafel slope also indicated that the rate-determining step over Co–P@NF was the dehydrogenation from $*N_2H_2$ to $*N_2H$. In addition, a comparison between the OER and HzOR performances over Co–P@NF was performed (Fig. 5c and d). Much lower potentials of 16 and 207 mV were needed in HzOR than those in N_2H_4-free electrolyte (1.66 and 1.95 V) to reach the current densities of 100 and 500 mA cm^{-2}, respectively, indicating the potential application to replace OER for HzOR-assisted NO_3^-RR. Therefore, thanks to the excellent NO_3^-RR and HzOR catalytic performances on Co–P@NF, an HzOR-assisted NO_3^-RR unit with two-electrode system was assembled by employing Co–P@NF as both anode and cathode. As shown in Fig. 5e, the HzOR-assisted NO_3^-RR unit exhibits significantly enhanced catalytic activity compared to the stand alone NO_3^-RR unit, only requiring voltages of 93, 308, and 516 mV to achieve current densities of 100, 300, and 500 mA cm^{-2}, respectively. These values are 1.45, 1.53, and 1.67 V lower than those required by the OER-assisted NO_3^-RR system. The cell voltage of Co–P@NF||Co–P@NF at 300 mA cm^{-2} dramatically dropped from *ca.* 2.0 V to *ca.* 0.34 V after addition of N_2H_4 in the electrolyte containing NO_3^- ions (Fig. 5f). For comparison, NF as electrodes for the HzOR-assisted NO_3^-RR unit was also assembled (Fig. S18†). For a current density of 300 mA cm^{-2}, and the cell voltage of NF||NF (2.40 V) are much higher than that of Co–P@NF||Co–P@NF (0.34 V), indicating the greatly reduced electricity consumption over Co–P catalysts.

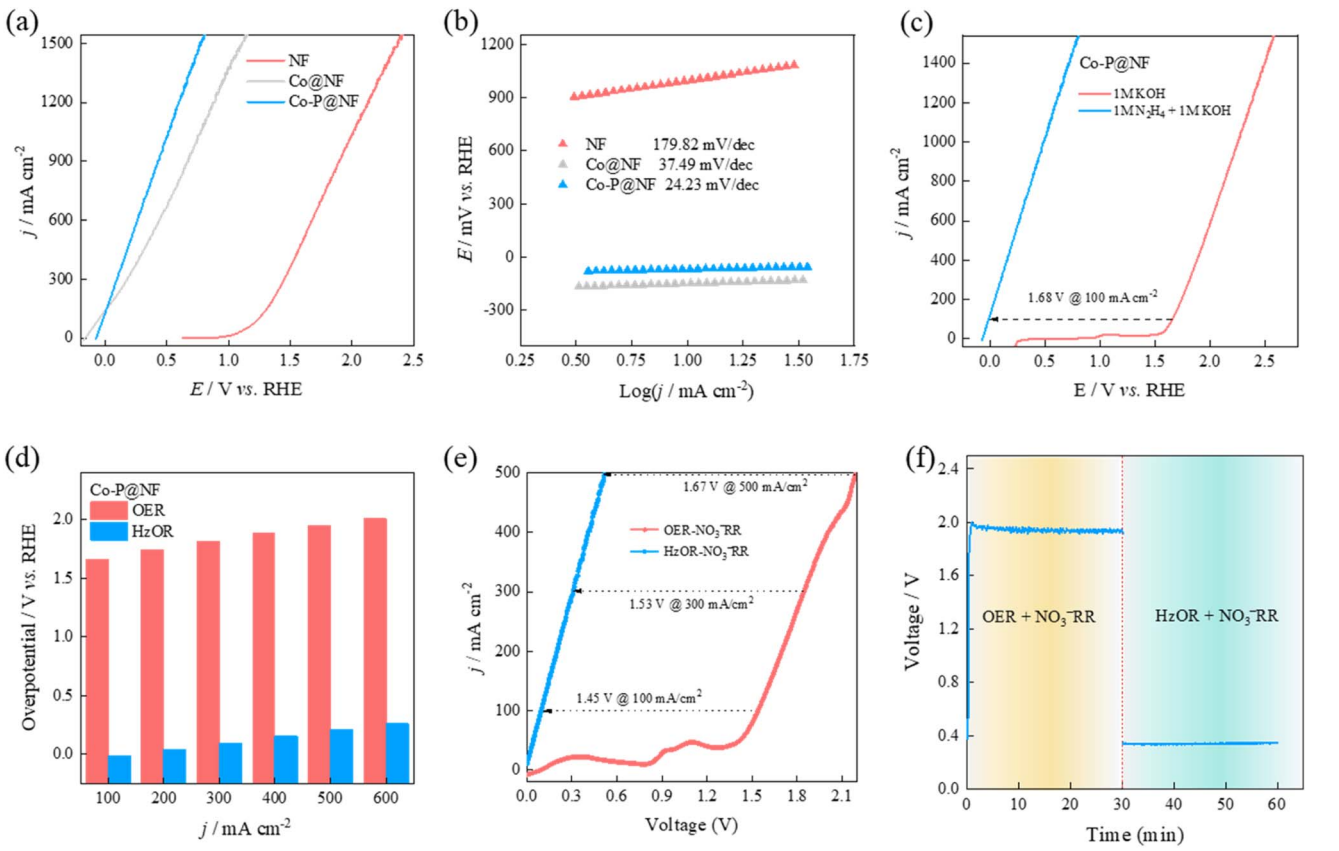

Fig. 5 HzOR performance in 1.0 M KOH + 1.0 M N_2H_4 electrolyte. (a) Linear sweep voltammetry analysis on NF, Co@NF and Co–P@NF catalysts and the corresponding (b) Tafel slopes. (c) Compared LSV curves of Co–P@NF between OER (1.0 M KOH) and HzOR (1.0 M KOH and 1.0 M N_2H_4), and (d) the corresponding histogram catalytic performance comparison. (e) Comparison LSV curves of Co–P@NF between OER-NO_3^-RR and HzOR-NO_3^-RR. (f) Cell voltage of Co–P@NF||Co–P@NF at 300 mA cm^{-2} in OER-NO_3^-RR and HzOR-NO_3^-RR system.

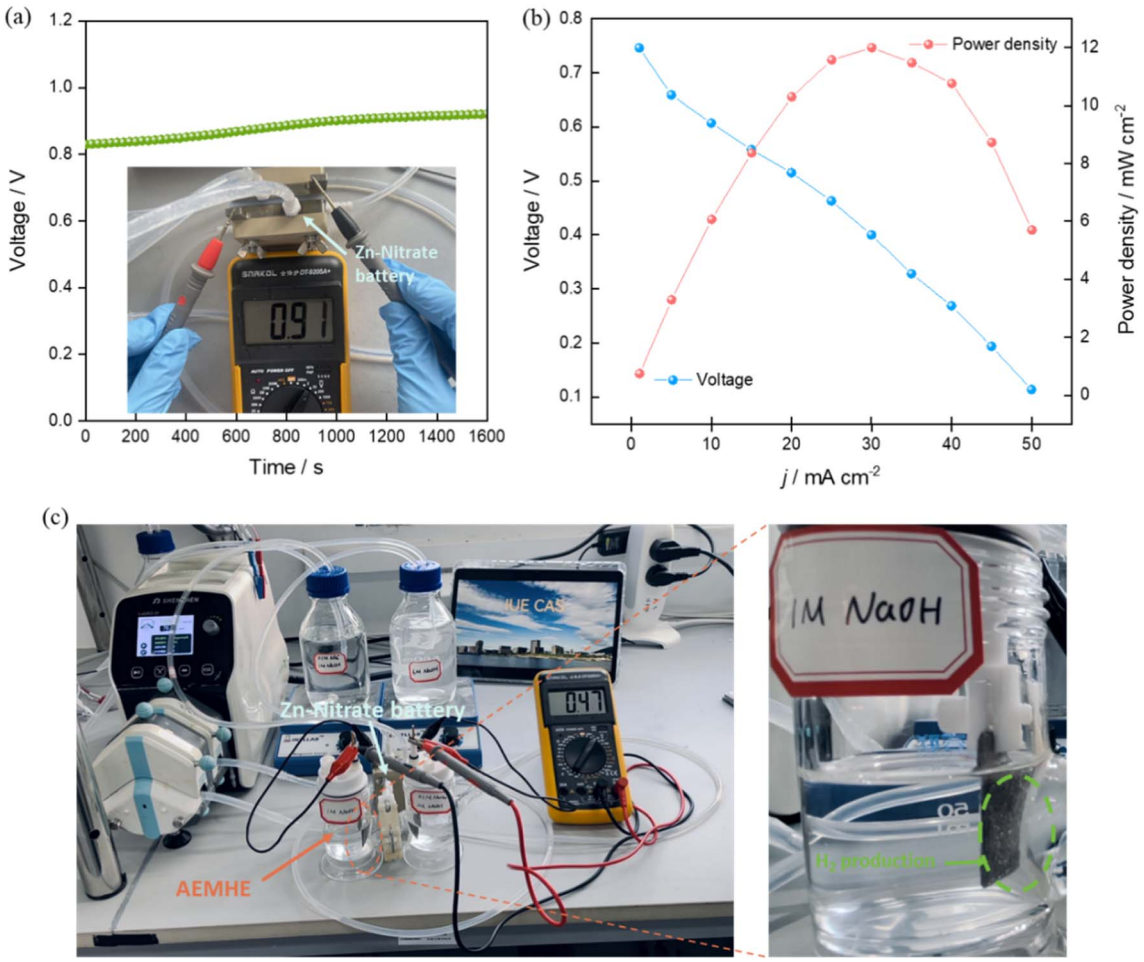

Fig. 6 Zn–nitrate flow battery application. (a) The open circuit voltage. The cathodic and anodic electrolytes used in Zn–nitrate flow battery were 0.1 M NO_3^- + 1 M NaOH and 6 M NaOH, respectively. (b) Polarization and power density curves. (c) The digital photograph of the tandem Zn–nitrate flow battery and AEMHE devices for hydrogen production.

The Zn–nitrate flow battery was assembled with an open circuit voltage over 0.8 V (Fig. 6a). The polarization curves by steady-state chronopotentiometry were obtained. The Zn–nitrate flow battery is practically feasible with the discharging power density up to 12 mW cm^{-2} (Fig. 6b). To confirm the efficacy of the electricity supply of this battery, the low-voltage-driven anion exchange membrane hydrazine electrolyzer (AEMHE), which used the bimetallic Co–P@NF as both the anode and cathode for the HzOR and HER, respectively (Fig. 6c). The Zn–nitrate flow battery can well drive the AEMHE with only a cell voltage of 0.47 V and give high current density over 35 mA cm^{-2} for H_2 production (Fig. S19†), the corresponding H_2 production rate as 0.64 mmol h^{-1} cm^{-2}. This result shows that the Zn–nitrate flow battery possesses great potential in electricity generation.

4. Conclusions

In summary, an amorphous P doped Co (Co–P@NF) was prepared *via* a facile electrodeposition process. Co–P@NF with a higher density oxygen vacancies sites showed high catalytic activities for both NO_3^-RR and HzOR. They show a high current density over 2 A cm^{-2} for NH_3 formation and high FE up to 91% at −0.3 V *versus* RHE in the electrolyte of 1 M NO_3^-. Thanks to the amorphous structure, the Co–P could preserve the oxygen vacancies sites and give a high stability for NO_3^- reduction over 82 h electrolysis with the current density over 799 mA cm^{-2} and the FE over 90%. A low cell voltage of HzOR-assisted NO_3^-RR at 300 mA cm^{-2} was also obtained over Co–P@NF‖Co–P@NF and was only 0.34 V. A Zn–nitrate flow battery was assemble using Co–P@NF as electrodes can deliver a peak power density of 12 mW cm^2 and well drive an AEMHE, accompanied with an H_2 yield rate of *ca.* 0.64 mmol h^{-1} cm^{-2}. This work demonstrates the feasibility for boosting the activity and stability toward NO_3^-RR by constructing the amorphous structure.

Data availability

All relevant data are within the manuscript and its additional files.

Author contributions

Jin-Long Fan: conceptualization, investigation, writing – original draft. Sheng-Bo Liu: investigation. Ming-Liang Chen:

writing – review & editing. Zhangxiong Wu: writing – review & editing. Sheng-Peng Sun: investigation, supervision. Yao-Yin Lou: conceptualization, investigation, supervision, writing – review & editing.

Conflicts of interest

No potential conflicts of interest were reported by the authors.

Acknowledgements

This research was financially supported by National Natural Science Foundation of China (NSFC) (No. 22002131) and China Postdoctoral Science Foundation (Grant No. 2020 M671963).

References

1 L. K. Boerner, Industrial ammonia production emits more CO_2 than any other chemical-making reaction. Chemists want to change that, *Chem. Eng. News*, 2019, **97**, 1–9.
2 S. Ye, *et al.*, Elucidating the activity, mechanism and application of selective electrosynthesis of ammonia from nitrate on cobalt phosphide, *Energy Environ. Sci.*, 2022, **15**, 760–770, DOI: **10.1039/D1EE03097C**.
3 X. Liu, A. Elgowainy and M. Wang, Life cycle energy use and greenhouse gas emissions of ammonia production from renewable resources and industrial by-products, *Green Chem.*, 2020, **22**, 5751–5761, DOI: **10.1039/D0GC02301A**.
4 Q. Hu, *et al.*, Reaction intermediate-mediated electrocatalyst synthesis favors specified facet and defect exposure for efficient nitrate–ammonia conversion, *Energy Environ. Sci.*, 2021, **14**(9), 4989–4997, DOI: **10.1039/D1EE01731D**.
5 J. Gao, *et al.*, Electrocatalytic Upcycling of Nitrate Wastewater into an Ammonia Fertilizer via an Electrified Membrane, *Environ. Sci. Technol.*, 2022, **56**, 11602–11613, DOI: **10.1021/acs.est.1c08442**.
6 G. Wen, *et al.*, Ambient ammonia production via electrocatalytic nitrite reduction catalyzed by a CoP nanoarray, *Nano Res.*, 2021, **15**(2), 972–977, DOI: **10.1007/s12274-021-3583-9**.
7 R. Zhang, *et al.*, Efficient Ammonia Electrosynthesis and Energy Conversion through a Zn-Nitrate Battery by Iron Doping Engineered Nickel Phosphide Catalyst, *Adv. Energy Mater.*, 2022, 2103872, DOI: **10.1002/aenm.202103872**.
8 J. Zhou, *et al.*, Linear Adsorption Enables NO Selective Electroreduction to Hydroxylamine on Single Co Sites, *Angew. Chem., Int. Ed.*, 2023, e202305184, DOI: **10.1002/anie.202305184**.
9 Z. Zhang, *et al.*, Electrochemical-catalytic reduction of nitrate over Pd-Cu/gamma Al_2O_3 catalyst in cathode chamber: Enhanced removal efficiency and N-2 selectivity, *Chem. Eng. J.*, 2016, **290**, 201–208, DOI: **10.1016/j.cej.2016.01.063**.
10 G., S. Renewable, Energy to Fuels through Utilization of Energy Dense Liquids (REFUEL) [EB/OL].
11 N. K. Oh, *et al.*, Highly efficient and robust noble-metal free bifunctional water electrolysis catalyst achieved via complementary charge transfer, *Nat. Commun.*, 2021, **12**, 4606, DOI: **10.1038/s41467-021-24829-8**.
12 L. Wei, D.-J. Liu, B. A. Rosales, J. W. Evans and J. Vela, Mild and Selective Hydrogenation of Nitrate to Ammonia in the Absence of Noble Metals, *ACS Catal.*, 2020, **10**, 3618–3628, DOI: **10.1021/acscatal.9b05338**.
13 P. Liu and J. A. Rodriguez, Catalysts for hydrogen evolution from the [NiFe] hydrogenase to the Ni_2P (001) surface: the importance of ensemble effect, *J. Am. Chem. Soc.*, 2005, **127**, 14871–14878.
14 B. Yang, *et al.*, Electron-deficient cobalt nanocrystals for promoted nitrate electrocatalytic reduction to synthesize ammonia, *Nano Energy*, 2023, **117**, 108901, DOI: **10.1016/j.nanoen.2023.108901**.
15 J. Li, *et al.*, Efficient Ammonia Electrosynthesis from Nitrate on Strained Ruthenium Nanoclusters, *J. Am. Chem. Soc.*, 2020, **142**, 7036–7046, DOI: **10.1021/jacs.0c00418**.
16 J.-Y. Fang, *et al.*, Ampere-level current density ammonia electrochemical synthesis using CuCo nanosheets simulating nitrite reductase bifunctional nature, *Nat. Commun.*, 2022, **13**, 7899.
17 B. K. Simpson and D. C. Johnson, Electrocatalysis of Nitrate Reduction at Copper-Nickel Alloy Electrodes in Acidic Media, *Electroanalysis*, 2004, **16**, 532–538.
18 Q. Fu, *et al.*, Unraveling and leveraging in situ surface amorphization for enhanced hydrogen evolution reaction in alkaline media, *Nat. Commun.*, 2023, **14**, 6462, DOI: **10.1038/s41467-023-42221-6**.
19 X. Li, *et al.*, Amorphous alloys for electrocatalysis: The significant role of the amorphous alloy structure, *Nano Res.*, 2023, **16**, 4277–4288, DOI: **10.1007/s12274-021-3682-7**.
20 M. Liu, Z. Zhao, X. Duan and Y. Huang, Nanoscale structure design for high-performance Pt-based ORR catalysts, *Adv. Mater.*, 2019, **31**, 1802234.
21 Y. X. Duan, *et al.*, Amorphizing of Cu nanoparticles toward highly efficient and robust electrocatalyst for CO_2 reduction to liquid fuels with high faradaic efficiencies, *Adv. Mater.*, 2018, **30**, 1706194.
22 Y. C. Hu, *et al.*, A highly efficient and self-stabilizing metallic-glass catalyst for electrochemical hydrogen generation, *Adv. Mater.*, 2016, **28**, 10293–10297.
23 J. Wang, *et al.*, Recent progress in cobalt-based heterogeneous catalysts for electrochemical water splitting, *Adv. Mater.*, 2016, **28**, 215–230.
24 S.-E. Bae, K. L. Stewart and A. A. Gewirth, Nitrate adsorption and reduction on Cu (100) in acidic solution, *J. Am. Chem. Soc.*, 2007, **129**, 10171–10180.
25 E. Molodkina, *et al.*, Electroreduction of nitrate ions on Pt (1 1 1) electrodes modified by copper adatoms, *Electrochim. Acta*, 2010, **56**, 154–165.
26 S. Han, *et al.*, Ultralow overpotential nitrate reduction to ammonia via a three-step relay mechanism, *Nat. Catal.*, 2023, **6**(5), 402–414, DOI: **10.1038/s41929-023-00951-2**.
27 P. H. van Langevelde, I. Katsounaros and M. T. M. Koper, Electrocatalytic Nitrate Reduction for Sustainable Ammonia Production, *Joule*, 2021, **5**, 290–294, DOI: **10.1016/j.joule.2020.12.025**.

28 J.-X. Liu, D. Richards, N. Singh and B. R. Goldsmith, Activity and Selectivity Trends in Electrocatalytic Nitrate Reduction on Transition Metals, *ACS Catal.*, 2019, **9**, 7052–7064, DOI: **10.1021/acscatal.9b02179**.

29 T. Begildayeva, J. Theerthagiri, S. J. Lee, Y. Yu and M. Y. Choi, Unraveling the Synergy of Anion Modulation on Co Electrocatalysts by Pulsed Laser for Water Splitting: Intermediate Capturing by In Situ/Operando Raman Studies, *Small*, 2022, **18**, 2204309, DOI: **10.1002/smll.202204309**.

30 J. Kang, *et al.*, Recent Progress of Amorphous Nanomaterials, *Chem. Rev.*, 2023, **123**, 8859–8941, DOI: **10.1021/acs.chemrev.3c00229**.

31 J. Wang, *et al.*, Electrocatalytic Reduction of Nitrate to Ammonia on Low-Cost Ultrathin CoOx Nanosheets, *ACS Catal.*, 2021, **11**, 15135–15140, DOI: **10.1021/acscatal.1c03918**.